Chapter 8

Fractal-Surface-Enhanced Optical Nonlinearities

V. M. Shalaev[1], V. P. Safonov[2], E. Y. Poliakov[1], V. A. Markel[1], and A. K. Sarychev[3]

[1]Department of Physics, New Mexico State University, Las Cruces, NM 88003
[2]Institute of Automation and Electrometry, Novosibirsk 630090, Russia
[3]Center for Applied Problems of Electrodynamics, Moscow 127412, Russia

Optical excitations of nanomaterials with fractal structure result in highly localized areas of large fields leading to strong enhancements of optical nonlinearities. The localized modes of fractals cover a broad spectral range, from the visible to the far-infrared.

Optical phenomena experience giant enhancements in metal nanocomposites and rough thin films consisting of small nanometer-sized particles and roughness features, respectively. The enhancement is associated with excitation of surface plasmons which are collective modes and strongly depend on the morphology (geometrical structure) of the material. Fractal structures are prevalent in composites and rough thin films. The emergence of fractal geometry was a significant breakthrough in the description of irregularity. Fractal objects do not possess translational invariance and, therefore, cannot transmit running waves. Accordingly, collective excitations, such as surface plasmons, tend to be localized in fractals (*1,2*). Formally, this is a consequence of the fact that plane running waves are not eigenfunctions of the operator of dilation symmetry characterizing fractals.

In fractals, collective plasmon oscillations are strongly affected by the fractal morphology, leading to the existence of "hot" and "cold" spots (i.e., areas of high and low local fields). It is interesting to note that in many cases local enhancements in the "hot spots" exceed the average surface enhancement by many orders of magnitude; this is because the local peaks of the enhancement are spatially separated by distances much larger than the peak sizes. Also, the spatial distribution of these high-field regions are very sensitive to the frequency and polarization of the applied field (*2-6*). The positions of the "hot spots" change chaotically but reproducibly with frequency or/and polarization. This is similar to speckle created by laser light scattered from a rough surface with the important difference that the scale-size for fractal plasmons in the hot spots is in the nanometer range rather than in the micrometer range for photons.

Two varieties of surface plasmons are commonly recognized: localized surface plasmons (LSP) and surface plasmon waves (SPW). [SPW are also called surface plasmon polaritons (SPP) - coherent mixture of plasmons and photons.] SPW propagate laterally along a metal surface whereas LSP are confined to metal

particles that are much smaller in size than the wavelength of the incident light. However, in fractal media plasmon oscillations in different features strongly interact with each other via dipolar or, more generally, multipolar forces. Thus, plasmon oscillations on a self-affine surface and in a fractal aggregate are neither conventional SPW nor independent LSP. Rather, they should be treated theoretically as collective eigenmodes arising from multipolar interactions in a fractal object.

With the aid of well-established chemical and depositional methods, fractal nanostructured materials may be fabricated. For example, colloidal clusters may be grown possessing a measured fractal dimension, 1.78 (*7*). Alternatively, fractals may be grown by particle-cluster aggregation (termed Witten-Sander aggregation or WSA (*7*)), having the fractal dimension, 2.5. Also, by controlling conditions of atomic beam deposition and substrate temperature, self-affine thin films may be grown with various fractal dimensions (*8*). Finally, metal-dielectric films (called also semicontinuous metal films) produced by metal sputtering onto an insulating substrate also include fractal clusters of metal granules near the percolation threshold (*7,8*).

The fractal plasmon, as any wave, is scattered from fluctuations of density (or, in other words, fluctuations of polarization). The strongest scattering occurs from inhomogeneities of the same scale as the wavelength. In this case, interference in the process of multiple scattering results in Anderson localization. Anderson localization corresponds typically to uncorrelated disorder. A fractal structure is in some sense disordered, but it is also correlated for all length scales, from the size of constituent particles, in the lower limit, to the total size of the fractal, in the upper limit. Thus, what is unique for fractals is that because of their scale-invariance, there is no characteristic size of inhomogeneity; inhomogeneities of all sizes are present from the lower to the upper limit. Therefore, whatever the plasmon wavelength, there are always fluctuations in a fractal with similar sizes, so that the plasmon is always strongly scattered and, consequently, localized (*2,9*).

Surface-Enhanced Optical Responses

Below we consider enhancement of optical responses on different fractal surfaces, such as aggregates of colloidal particles, self-affine thin films, and semicontinuous metal films in a vicinity of the percolation threshold. We assume that each site of the surface possesses a required nonlinear polarizability, in addition to the linear one. The local fields associated with the light-induced eigenmodes of a fractal surface can significantly exceed the applied macroscopic field, $\mathbf{E}^{(0)}$. For metal surfaces, this enhancement increases toward the infrared part of the spectrum where resonance quality-factors are significantly larger, in accordance with the Drude model of metal (*2,4*).

We begin our consideration with the Kerr-type nonlinearity, $\chi^{(3)}(-\omega;\omega,\omega,-\omega)$, that is responsible for nonlinear corrections to absorption and refraction. This type of optical nonlinearities can be in particular used for optical switches and optical limiters. The local nonlinear dipole, in this case, is proportional to

$|\mathbf{E}(\mathbf{r})|^2\mathbf{E}(\mathbf{r})$, where $\mathbf{E}(\mathbf{r})$ is the local field at the site $\mathbf{r}$. For the resonant eigenmodes, the local fields exceed the macroscopic (average) field by a quality-factor, q.

The fields generated by the nonlinear dipoles can also excite resonant eigenmodes of a fractal surface resulting in the additional "secondary" enhancement $\propto \mathbf{E}(\mathbf{r})/\mathbf{E}^{(0)}$. Accordingly, the surface-enhanced Kerr-susceptibility, $\bar{\chi}^{(3)}$, can be represented as (the angular brackets in the following formulas denote an ensemble-average) (*2,4,10*)

$$\bar{\chi}^{(3)}/p\chi^{(3)} = G_K = \frac{\left\langle \left|\mathbf{E}(\mathbf{r})\right|^2 \left[\mathbf{E}(\mathbf{r})\right]^2 \right\rangle}{\left[\mathbf{E}^{(0)}\right]^4}. \qquad (1)$$

Here $\chi^{(3)}$ is the initial "seed" susceptibility; it can be associated with some adsorbed molecules (then, $\bar{\chi}^{(3)}$ represent the nonlinear susceptibility of the composite material consisting of the adsorbed nonlinear molecules and a surface providing the enhancement). The seed $\chi^{(3)}$ can be also associated with an isolated colloidal particle; then, G_K represents the enhancement due to clustering initially isolated particles into aggregates, with the average volume fraction of metal given by p. The applied field with the frequency in the visible, near IR or IR parts of the spectrum is typically off resonance for an isolated colloidal particle (e.g., silver) but it does efficiently excite the eigenmodes of fractal aggregates of the particles; the fractal eigenmodes cover large frequency interval including the visible and infrared parts of the spectrum (*2,4*).

Note that definition (1) for G_K, as well as the definitions of other enhancement factors introduced in this paper, are generic, i.e., applicable to any surface or 3-dimensional cluster, irrespectively of their fractal nature. However, the fractality is important because it results in especially large values of these enhancement factors as we will see below.

For simplicity, we assume that $\mathbf{E}^{(0)}$ in (1) is linearly polarized and therefore can be chosen real. In Refs. (*4,6*), the above formula was proven from rigorous first-principle considerations. Note also that G_K depends on the local-field phases and it contains both real and imaginary parts.

Because of a random character of fractal surfaces the high local fields associated with the localized eigenmodes look like strong spatial fluctuations. Since a nonlinear optical process is proportional to the local fields raised to some high power the resultant enhancement associated with the fluctuation area ("hot" spot) can be extremely large. In a sense, one can say that enhancement of optical nonlinearities is especially large in fractals because of very strong field fluctuations.

Four-wave mixing (FWM) is determined by the nonlinear susceptibility similar to (1) $\chi^{(3)}_{\alpha\beta\gamma\delta}(-\omega_s;\omega_1,\omega_1,-\omega_2)$, where $\omega_s = 2\omega_1 - \omega_2$ is the generated frequency, and ω_1 and ω_2 are the frequencies of the applied waves. Coherent anti-Stokes Raman scattering (CARS) is an example of FWM. In one elementary CARS process, two ω_1 photons are transformed into the ω_2 and ω_s photons. Another example is degenerate FWM (DFWM); this process is used for optical phase conjugation (OPC) that can result in complete removal of optical aberrations (*11*). In DFWM, all waves have the same frequency ($\omega_s = \omega_1 = \omega_2$) and differ only by their propagation directions and, in general, by polarizations. In a typical OPC experiment, two oppositely directed pump beams, with field amplitudes $\mathbf{E}^{(1)}$ and $\mathbf{E}'^{(1)}$, and a probe beam, with amplitude $\mathbf{E}^{(2)}$ (and propagating at a small angle to the pump beams), result in a OPC beam which propagates against the probe beam. Because of the interaction geometry, the wave vectors of the beams satisfy to the relation: $\mathbf{k}_1 + \mathbf{k}'_1 = \mathbf{k}_2 + \mathbf{k}_s = 0$. Clearly, for the two pairs of oppositely directed beams, that have the same frequency ω, the phase-matching conditions are automatically fulfilled (*11*).

The nonlinear susceptibility, $\chi^{(3)}$, that results in DFWM, also leads to the considered above nonlinear refraction and absorption that are associated with the Kerr optical nonlinearity. Note also that as above the nonlinear susceptibility, $\chi^{(3)}$, can be associated with either the fractal surface itself or molecules adsorbed on the surface.

For coherent effects, including the ones discussed in this section, averaging is performed for the generated field amplitude (rather than intensity) or, equally, for the nonlinear polarization of a medium. The average polarization, $P^{(3)}(\omega)$, is proportional to the nonlinear susceptibility, $P^{(3)}(\omega) \propto \bar{\chi}^{(3)} = \chi^{(3)}G_K$. The measured signal for coherent processes is proportional to $|\bar{\chi}^{(3)}|^2$. Thus we conclude that the resultant enhancement for degenerate (or near degenerate) four-wave mixing can be expressed in terms of the enhancement for the Kerr susceptibility as follows (*4*)

$$G_{FWM} = \left|G_K\right|^2 = \left|\frac{\left\langle \left|\mathbf{E}(\mathbf{r})\right|^2 \left[\mathbf{E}(\mathbf{r})\right]^2 \right\rangle}{\left[\mathbf{E}^{(0)}\right]^4}\right|^2. \qquad (2)$$

Note that one can equally describe a medium optical response in terms of the nonlinear currents rather nonlinear polarizations; these two approaches are completely equivalent (*6*).

Raman scattering is a linear optical process. For small Stokes shifts, however, the surface-enhanced Raman scattering is proportional to the average of fourth power of the local fields (*4,12*), so that the corresponding enhancement factor is (*4*)

$$G_{RS} = \frac{\left\langle \left|\mathbf{E}(\mathbf{r})\right|^4 \right\rangle}{\left[\mathbf{E}^{(0)}\right]^4}. \qquad (3)$$

Note that in contrast to the enhanced Kerr nonlinearity considered above, G_{RS} is real and the local enhancement is phase insensitive, so that there is no destructive interference of signals from different points of a surface. As a result, typically, $G_{RS} \gg G_K$.

Under some simplifying conditions, the enhancement for the second harmonic generation can be written as (*2*)

$$G_{SHG} = \left|\left\langle \left[\frac{E_\omega(\mathbf{r})}{E_\omega^{(0)}}\right]^2 \left[\frac{E_{2\omega}(\mathbf{r})}{E_{2\omega}^{(0)}}\right] \right\rangle\right|^2, \qquad (4)$$

where $E_{2\omega}^{(0)}$ and $E_{2\omega}(\mathbf{r})$ are the macroscopic and local *linear* fields at frequency 2ω. If there is no enhancement at frequency 2ω, then $E_{2\omega}(\mathbf{r}) = E_{2\omega}^{(0)}$.

The above formula can be easily generalized for the n-th harmonic generation:

$$G_{nHG} = \left| \left\langle \left[\frac{E_\omega(\mathbf{r})}{E_\omega^{(0)}} \right]^n \left[\frac{E_{2\omega}(\mathbf{r})}{E_{2\omega}^{(0)}} \right] \right\rangle \right|^2. \qquad (5)$$

Note that the above formulas are valid for arbitrary surface fractal or non-fractal. In fractals, however, because of the extremely large field fluctuations the ensemble average enhancements are typically much larger than for non-fractal surfaces. In addition, the fractal modes provide enhancements in a very large spectral range including the infrared part, where the enhancement is particularly large because of the high quality-factor for metal surfaces in this spectral range (*2*). We will also show below that the local enhancements in the "hot" zones (associated with the localized eigenmodes) can exceed the ensemble-average enhancement by many orders of magnitude.

Fractal Aggregates of Colloidal Particles. As well known, there is only one dipolar mode that can be excited by a homogeneous field in a spherical object. For a 3-dimensional (non-fractal) collection of small particles, such as randomly close-packed hard spheres of particles (CPHS) or a random gas of particles (RGP), absorption spectra are peaked near the relatively narrow resonance of the individual particles, i.e., all eigenmodes of the collection of particles are located within a small spectral interval (*4*).

In contrast to such conventional (non-fractal) 3-dimensional systems, dipolar interactions in low-dimensional fractal clusters are not long range; this results in the spatial localization of the eigenmodes at various random locations in the cluster (*2-6,9*). The spectrum of these eigenmodes exhibits strong inhomogeneous broadening as a result of spatial variability of the local environment. It is also important to note that, despite the asymptotically zero mean density of particles in a fractal cluster, a high probability always exists of finding a number of particles in close proximity to a given particle (stated more precisely, in fractals, the pair correlation $g \propto r^{D-d}$ ($D < d$), where D is the fractal dimension and d is the dimension of the embedding space; accordingly, g becomes large at small r). Thus, objects with fractal morphology possess an unusual combination of properties; namely, despite the fact that the volume fraction filled by N particles in a fractal is very small, $\propto N^{1-d/D} \to 0$, strong interactions nevertheless exist between neighboring particles (*2*). These strong interactions between neighboring particles, which are highly variable because of variability of local particle configurations in the cluster, lead to the formation of inhomogeneously broadened eigenmodes covering a broad spectral range (*4*).

Localization of eigenmodes in fractals leads to a patchwork-like distribution of local fields associated with "hot" and "cold" zones (*2,3,9*). This, in turn, results in large spatial fluctuations of local fields in fractal composites and in the giant enhancement of various optical effects (*2-6,9*).

For the special case of fractals formed by metal particles, the dipole eigenmodes span the visible and infra-red regions of the spectrum; since the mode quality-factors increase with wavelength, local fields are especially large in the long wavelength part of the spectrum (*2,4*).

In Figure 1, we show an electron microscope picture of a typical aggregate of silver colloidal particles. The fractal dimension for these aggregates is $D \approx 1.78$. Using the well-known model of cluster-cluster aggregation, colloidal aggregates can be readily simulated numerically (*7*). Note that voids are presented in all scales from the minimum one (about the size of a single particle) to the maximum one (about the size of the whole cluster); this is indication of the statistical self-similarity of a fractal cluster. The size of an individual particle is $\sim$ 10 nm, whereas the size of the whole cluster is $\sim 1\mu$m.

In Figures 2a and 2b, we show results of our calculations for enhancement of the real, G'_K, and imaginary, G''_K (see formula(1)), parts of the enhancement of the Kerr-nonlinearity, and, in Figure 2c, the enhancement for the four-wave mixing, $G_{FWM} = |G_K|^2$, in silver colloidal aggregates. We use the experimental data for the optical constants of bulk silver from (*13*). The enhancements increase toward the infrared part of the spectrum where the resonance quality-factors are larger and the localization of the eigenmodes is stronger (*2,4*).

The nonlinear susceptibility, $\bar{\chi}^{(3)}$ of the composite material consisting of fractal aggregates of colloidal particles in solution is given by $\bar{\chi}^{(3)} = p \cdot G_K \chi_m^{(3)}$, where $\chi_m^{(3)}$ is the susceptibility of the non-aggregated colloidal particles and p is the volume fraction filled by metal. The experimentally measured value of $\chi_m^{(3)}$ re-estimated for $\lambda = 532$ nm is $\chi_m^{(3)} \approx 10^{-8}$ esu (*14*). As follows from Figure 2, $|G_K| \sim 10^4$ for $\lambda = 532$ nm. With the indicated value of $\chi_m^{(3)}$ and $p \approx 5 \cdot 10^{-6}$ used in our experiments, we obtain $|\bar{\chi}^{(3)}| \approx 5 \cdot 10^{-10}$ esu. This is in good agreement with the experimentally (using the degenerate four-wave mixing) obtained value, $|\bar{\chi}^{(3)}| = 5.7 \cdot 10^{-10}$ esu (*15*).

Note that p is a variable quantity and can be increased. We can assign the value 10^{-4} esu to the nonlinear susceptibility, $\chi^{(3f)}$, of fractal aggregates, i.e., $\bar{\chi}^{(3)} = p \cdot \chi^{(3f)}$, with $\chi^{(3f)} \sim 10^{-4}$ esu. This is a very large value for a third-order nonlinear susceptibility.

The above high nonlinearities were obtained at the pump intensity $I_L \leq 1.5$ MW/cm^2. At higher intensities a light-induced modification (selective in frequency and polarization) occurs resulting in local re-structuring of resonant domains (hot spots) in the irradiated cluster; this in turn leads to a dip in the aggregate absorption spectrum in the vicinity of laser wavelength (*15,16*).

In the other series of experiments, using Z-scan technique, both nonlinear refraction and absorption were measured (*16*). It has been found that for $\lambda = 540nm$ and $p = 5 \cdot 10^{-6}$, the aggregation of silver colloidal particles into fractal clusters is accompanied by the increase of the nonlinear correction, α_2, to the absorption, $\alpha(\omega) = \alpha_0 + \alpha_2 I$, from $\alpha_2 = -9 \cdot 10^{-10}$ cm/W to $\alpha_2 = -5 \cdot 10^{-7}$ cm/W, i.e., the enhancement factor is 560 (*16*). The measured nonlinear refraction at $\lambda = 540nm$ for fractal aggregates of silver colloidal particles is $n(\omega) = n_0 + n_2 I$, with $n_2 = 2.3 \cdot 10^{-12}$ cm^2/W. Similar measurments at $\lambda = 1079$ nm give the following values $n_2 = -0.8 \cdot 10^{-12}$ cm^2/W and $\alpha_2 = -0.7 \cdot 10^{-7}$ cm/W.

The measured n_2 and α_2 allows one to find the real and imaginary parts of the Kerr susceptibility; they are $Re[\bar{\chi}^{(3)}] = 1 \cdot 10^{-10}$ esu, $Im[\bar{\chi}^{(3)}] = -0.8 \cdot 10^{-10}$

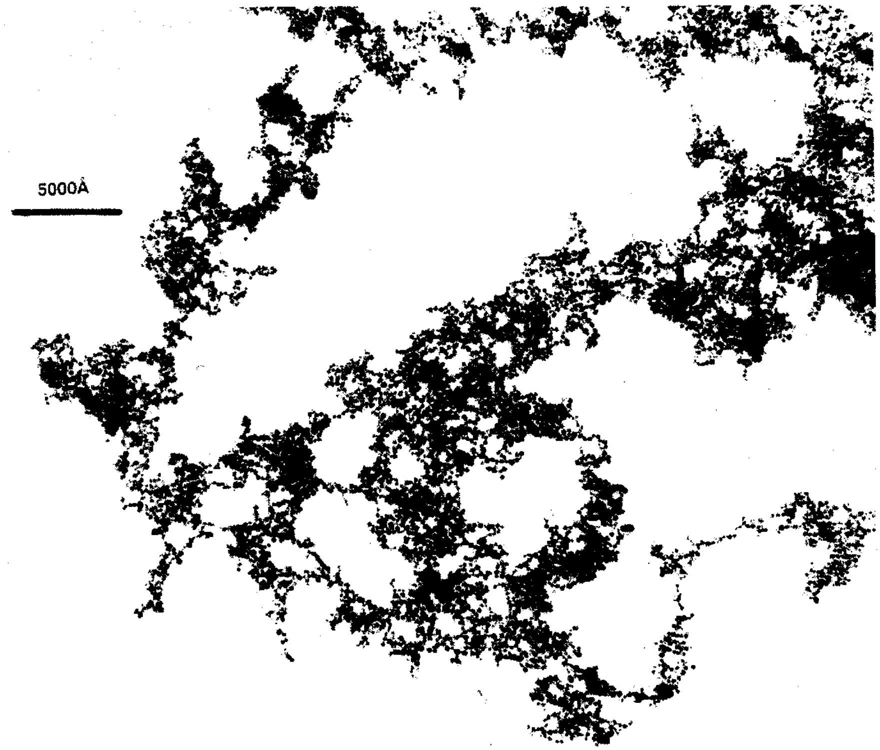

Figure 1. Electron micrograph of a silver cluster-cluster aggregate (CCA).

a)

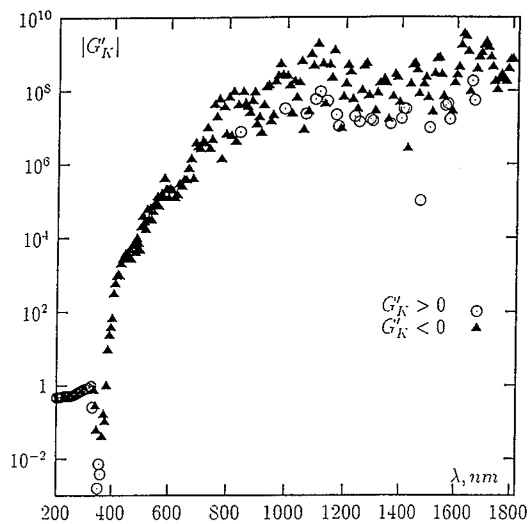

Figure 2. Enhancements on silver CCAs for the real, G'_K, (a) and imaginary, G''_K, (b) parts of the Kerr-type optical nonlinearity and for four-wave mixing, G_{FWM}, process (c).

b)

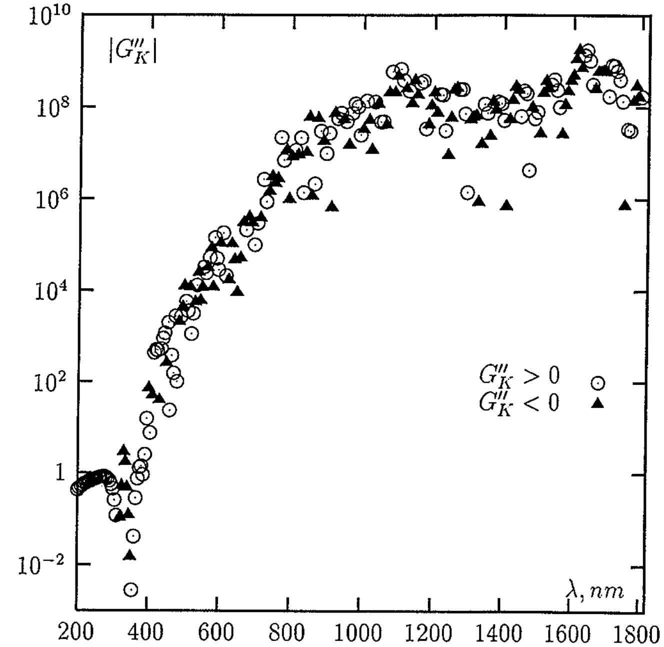

c)

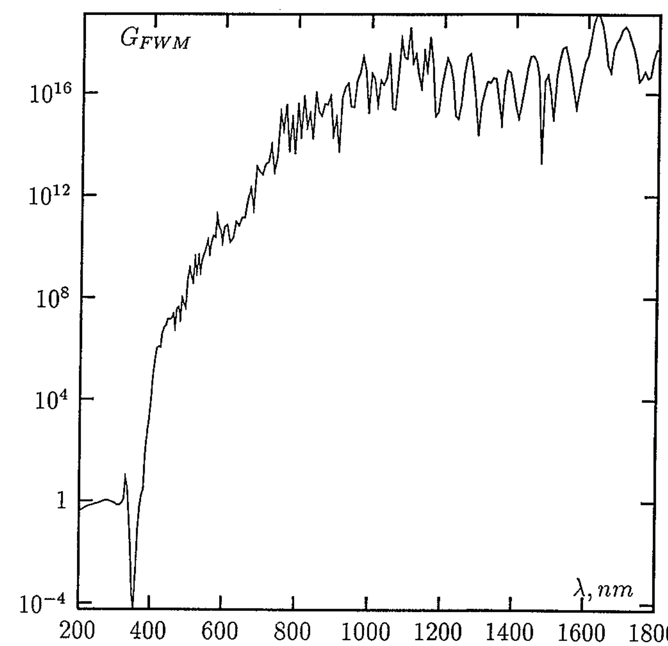

Figure 2. *Continued.*

esu, for $\lambda = 540nm$, and $Re[\bar{\chi}^{(3)}] = -3.5 \cdot 10^{-11}$ esu, $Im[\bar{\chi}^{(3)}] = -2.7 \cdot 10^{-11}$, for $\lambda = 1079$ nm. This means that the saturation of absorption and the nonlinear refraction provide comparable contributions to the nonlinearity. Note that the real part changes its sign with the wavelength.

Using a different technique based on a dispersion interferometer, the nonlinear correction to the refractive index, n_2, was also measured for $\lambda = 1064$ nm (at $p = 5 \cdot 10^{-6}$ and the intensity below the photomodification threshold); the obtained value is $n_2 = -1.5 \cdot 10^{-11}$ cm^2/W that corresponds to $Re[\bar{\chi}^{(3)}] \approx -7 \cdot 10^{-10}$ esu (*16*).

Note that fractal aggregates of colloidal particles can be placed into polymer or gel matrices. Thin films can then be prepared with fractal aggregates in such matrices. The volume fraction filled by metal fractal aggregates in such thin films is typically larger than in the case of colloidal solution and therefore the nonlinearities are significantly higher.

The laser pulse duration used in the above experiments was $\sim 10ns$. The Kerr type third-order nonlinearity was also detected with the use of 30 ps laser pulses; however, the observed optical nonlinearities were in this case significantly smaller than in the experiments with ns laser pulses. Our studies indicate that there are probably two different types of the optical nonlinearities, $\bar{\chi}^{(3)}$. A smaller one has the time of nonlinear response in the picosecond scale and a larger one in the nanosecond scale. The first one is associated with polarization of metal particles in an aggregate, whereas the second one probably involves absorption-related effects resulting in a holographic grating in colloidal clusters.

We also mention that very high optical susceptibilities, $|\bar{\chi}^{(3)}| \approx 10^{-6}$ esu with a subpicosecond response time was recently obtained for films containing J-aggregates of a dye (PIC) in a PVP matrix when fractal clusters of gold or silver are added to it (*17*).

We mention that rather strong enhancements of optical nonlinearities were obtained in non-fractal composite materials as well (*18*).

To conclude this section, we also show in Figure 3 results of our theoretical calculations and experimental studies of SERS in fractal aggregates of silver colloidal particles (*4,12*). As seen from the figure, the theory successfully explains the experimental observations. Note that the enhancement increases toward the red part of the spectrum, where the local fields associated with the localized fractal modes are significantly larger.

Self-Affine Thin Films. We also performed studies of linear and nonlinear optical properties of self-affine thin films. Rough thin films, formed when an atomic beam condenses onto a low-temperature substrate, are typically self-affine fractal structures (*8*). Contrary to the case of "usual" roughness, there is no correlation length for self-affine surfaces, which implies that inhomogeneities of all sizes are present (within a certain size interval) according to a power-law distribution. Self-affine surfaces obtained in the process of film growth belong to the Kardar-Parisi-Zhang universality class. Unlike statistically self-similar structures, to reveal scale-invariance, a self-affine surface (SAS) requires different scaling factors in the (x, y)-plane and in the normal direction, z.

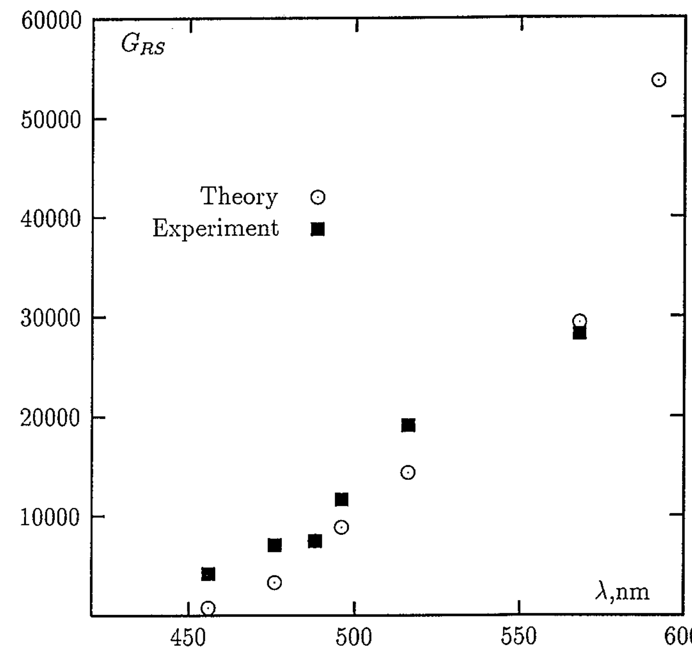

Figure 3. Theoretical and experimental enhancement factors, G_{RS}, for silver colloid aggregates as a function of the wavelength.

To simulate a self-affine film, we used the restricted solid-on-solid (RSS) model (for details see (*5*) and references therein). In this model, a particle is incorporated into the growing aggregate only if the newly created interface does not have steps which are higher than one lattice unit, a. The surface structure of such deposits is relatively simple, because there are no overhangs. In this way strong corrections to scaling effects are eliminated and the true scaling behavior appears clearly, even for small dimensions. In the long-time regime, the height-height correlation function for a self-affine surface has the form

$$\langle [h(\mathbf{R}) - h(0)]^2 \rangle \sim R^{2H},$$

where $\mathbf{R}$ is the radius-vector in the plane normal to the growth direction, z, and the scaling exponent (co-dimension), H, is related to the fractal dimension, D, through the formula $H = 3 - D$. For the RSS model, $D = 2.6$ and the scaling formula above is valid for large values of the average height, $\bar{h}$, (which is proportional to the deposition time), such that $\bar{h} \gg l^{\zeta}$, where $\zeta = 2(d+1)/(d+2) = 2 - H$ (l is the linear size of a system and d is the dimension of the embedding space. Our simulations satisfied this condition, and the above scaling relation was well pronounced.

Our analysis revealed that the eigenmodes of a self-affine film possess strongly inhomogeneous spatial distributions characterized by various degrees of localization (*5*). On a metal self-affine film, the intensities in areas of high local fields ("hot" zones) exceed the applied field intensity by approximately three orders of magnitude in the visible part of the spectrum. In common with the mode-structure of fractal aggregate media, the spatial locations of "hot" zones on a self-affine thin film are very strong functions of the frequency and polarization of the incident light.

In Figure 4a, we show a computer-generated self-affine film obtained within the restricted solid-on-solid model ($D = 2.6$); the model provides an accurate description for *Ag* cold-deposited films having approximately the same fractal dimension (*8*).

The importance of field localization in accounting for the optical properties of self-affine surfaces have recently been demonstrated experimentally by the University of Toronto research team led by Prof. M. Moskovits (*19*). Self-affine fractal surfaces were prepared by gravitationally depositing fractal aggregates of colloidal silver particles out of solution onto pyrex microscope cover-slides. Thick deposits were prepared in order to ensure a self-affine structure. Our numerical simulation of this process showed that the surface resulting from deposition of many clusters on top of each other is self-affine with the fractal dimension $D \approx 2.5$.

Note that a similar strong dependence on frequency and polarization of the applied field was also obtained in previous experiments on near-field scanning optical microscopy of localized optical modes in *Ag* fractal aggregates deposited onto a surface (*3*).

In Figure 4b, we show results of our theoretical calculations for the average enhancement of Raman scattering for both small and large Stokes shifts on self-affine films generated in the RSS model. $G_{RS,\parallel}$ and $G_{RS,\perp}$ describe enhancements

a)

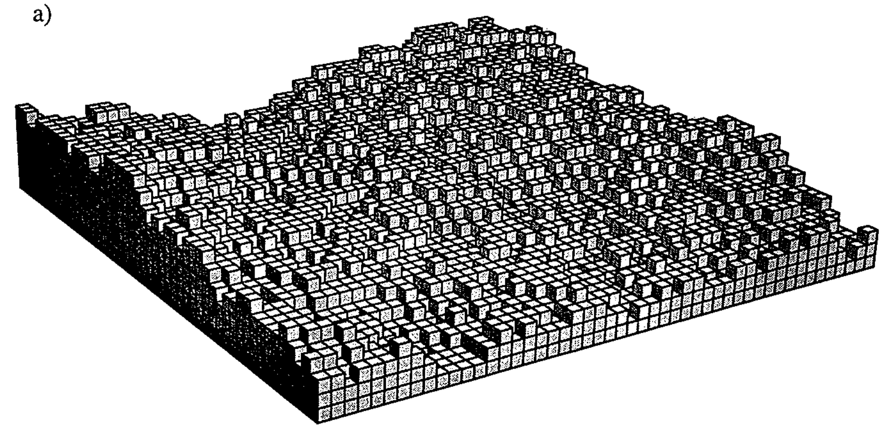

b)

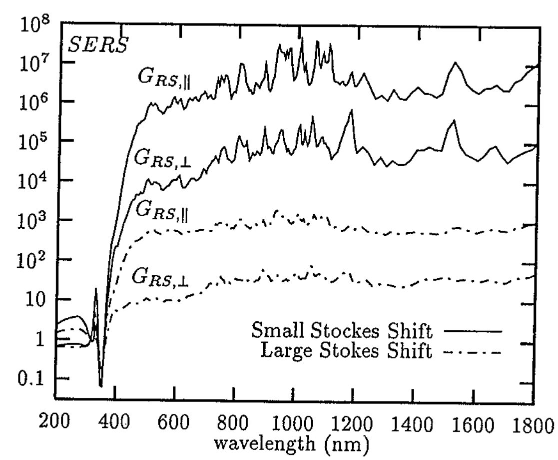

Figure 4. (a) Self-affine film obtained in the restricted solid-on-solid model. (b) The enhancement of Raman scattering on silver self-affine films for the applied field polarized in the plane of the film ($G_{RS,\parallel}$) and normal to the plane ($G_{RS,\perp}$) for small and large Stokes shifts.

for the applied field polarized in the plane of the film and perpendicular to it, respectively. As seen in the figure, the enhancement increases toward the long-wavelength part of the spectrum and reaches very large values, $\sim 10^7$; this agrees well with the experimental observations of SERS on cold-deposited thin films (*12*).

In Figures 5 a-c, the field spatial distributions at the fundamental and Stokes frequencies are shown. As seen in the figure, the distributions contain "hot" spots, where the fields are very high. Although the Stokes signal is proportional to the local field at the fundamental frequency, ω, the generated Stokes field, with frequency ω_s, excites, in general, other eigenmodes. Hence the field spatial distributions produced by the applied field and by the Raman signal can be different, as clearly seen in the figure.

This pattern is expected to be typical for various optical processes in strongly disordered fractal systems, such as self-affine thin films. Specifically, hot spots associated with fields at different frequencies and polarizations can be localized in spatially separated nm-sized areas. These novel nano-optical effects can be probed with NSOM providing sub-wavelength resolution (*3,19*).

If molecules possess the nonlinear susceptibility, $\chi^{(2)}$, then second harmonic generation (SHG) can be strongly enhanced when adsorbing the molecules on a metal self-affine surface. In Figure 6, we plot the calculated enhancement for SHG from molecules on a silver self-affine surface (for the applied field polarized parallel and perpendicular to the surface, $G_{SHG,\|}$ and $G_{SHG,\perp}$, respectively). To calculate the enhancements we used formula (4). As seen in the figure, the enhancement is very large and increases toward larger wavelengths.

Semicontinuous Metal Films. Self-affine thin films are typically produced by condensing atomic beams onto a *low-temperature* substrate. When placed into the air at room temperatures these films are annealed and change their morphology, yet remaining random. Our preliminary calculations showed that such annealed films produced originally at low-temperature still provide large enhancement of local fields, however, the spectral range where the enhancement occurs is somewhat narrowed.

For applications, it is important to have fractal films that retain their fractal morphology at room temperatures, such as two-dimensional semicontinuous metal films near the percolation threshold. In the vicinity of this threshold, fractal clusters are formed from metal granules (produced by thermal evaporation or sputtering of metal onto an insulator substrate). In contrast to self-affine films that are essentially 3-dimensional, the 2-dimensional semicontinuous films remain stable at room temperatures.

In the growing process of metal semicontinuous films, small metallic grains are first formed on the substrate. As the film grows, the metal filling factor increases and coalescences occur, so that irregularly shaped clusters are formed on the substrate eventually resulting in $2d$ fractal structures. The sizes of these structures diverge in the vicinity of the percolation threshold. A percolating cluster of metal is eventually formed, when a continuous conducting path appears between the ends of a sample. The metal-insulator transition (in other words, the conductivity threshold) is very close to this point.

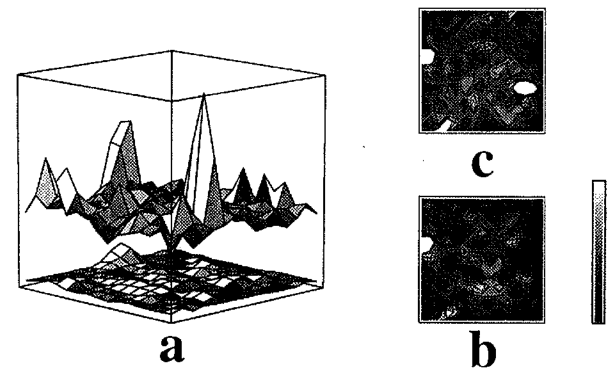

Figure 5. a): The spatial distributions for the local fields at the fundamental frequency, $\lambda = 550nm$, (bottom; the field distribution is magnified by 3) and for the Stokes fields, $\lambda_s = 600nm$, (top). [The applied field is linearly polarized in the plane of the film.] b) and c) : The contour-plots for the field distributions shown on a).

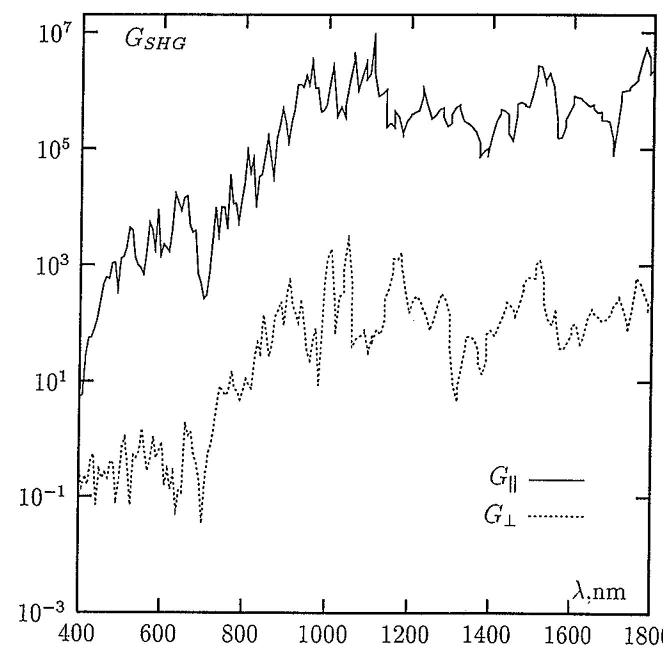

Figure 6. The enhancement for second harmonic generation, G_{SHG}, on the self-affine silver surface for the applied field polarized in the plane, $G_{\|}$, and normal to the plane, $G_{\perp}$.

We showed that SERS from Raman active molecules adsorbed onto a semi-continuous films in the vicinity of the percolation threshold is given by (*6*)

$$G_{RS} = \frac{\left\langle \left|\varepsilon(\mathbf{r})\right|^2 \left|\mathbf{E}(\mathbf{r})\right|^4 \right\rangle}{\varepsilon_d^2 \left[\mathbf{E}^{(0)}\right]^4} \approx 9.5 \frac{|\varepsilon_m'|^3}{\varepsilon_d \varepsilon_m''}, \tag{6}$$

where ε is the dielectric constant of the film consisting of a dielectric substrate, with $\varepsilon = \varepsilon_d$, and metal metal grains, with $\varepsilon = \varepsilon_m = \varepsilon_m' + i\varepsilon_m''$. The second approximate equality in (6) was obtained using the scaling analysis (*6*). Note that formula (6) differs from (3) by factor $\left|\varepsilon(\mathbf{r})/\varepsilon_d\right|^2$; the difference results from the fact that in (3) we assumed that both the Raman and linear polarizabilities are associated with the same site on a fractal surface, whereas to obtained (6) we supposed that the linear polarizability is due to a metal grain on the film but the Raman polarizability is due to a molecule adsorbed on the grain.

In Figure 7 we show results of our Monte Carlo simulations for Raman scattering from a silver semicontinuous film at the percolation threshold (based on the first equality in (6)) and results of the calculations based on the approximate scaling formula (second equality in (6)). One can see that the scaling formula works well for almost all frequencies, except the small frequencies that are comparable or smaller than the relaxation constant.

In Figure 8 we show distributions of the local Raman signals on a silver semicontinuous film at $p = p_c$, for different wavelengths, $\lambda = 1.5\mu m$ and $\lambda = 10\mu m$. As seen in the figure, the Stokes field intensities have the forms of sharp peaks sparsely distributed on the film, with the magnitudes increasing toward the long-wavelength part of the spectrum. The local enhancement in peaks achieve 10^9, for $\lambda = 1.5\mu m$, and 10^{12}, for $\lambda = 10\mu m$. [The Raman signal distributions were calculated using the first formula in (6) but with no averaging over samples (so that the sign $< .. >$ should be omitted in this case).] The average enhancement, G_{RS}, is much less, of the order of 10^6, for both wavelengths (see Figure 7). As seen in Figure 8, the peak positions strongly depend on the frequency. This non-trivial pattern for the local SERS distribution can be probed by means of near-field optical microscopy. If the density of Raman-active molecules is small so that it approximately equals to the surface concentration of the metal grains on the film, then each peak in Figure 8 is due to Raman scattering from a *single* molecule. Thus the presented picture of the SERS distribution opens an unique opportunity to perform Raman spectroscopy of a single molecule on a semicontinuous metal film.

Let molecules, possessing the nonlinear susceptibility $\chi^{(2)}(-2\omega;\omega,\omega)$, be adsorbed on a dielectric substrate; then the adding metal grains on the film results in enhancement of the second-harmonic generation by factor:

$$G_{SHG} = \left| \left\langle \frac{\varepsilon_{2\omega}(\mathbf{r})}{\varepsilon_{d,2\omega}} \left[\frac{E_\omega(\mathbf{r})}{E_\omega^{(0)}}\right]^2 \left[\frac{E_{2\omega}(\mathbf{r})}{E_{2\omega}^{(0)}}\right] \right\rangle \right|^2, \tag{7}$$

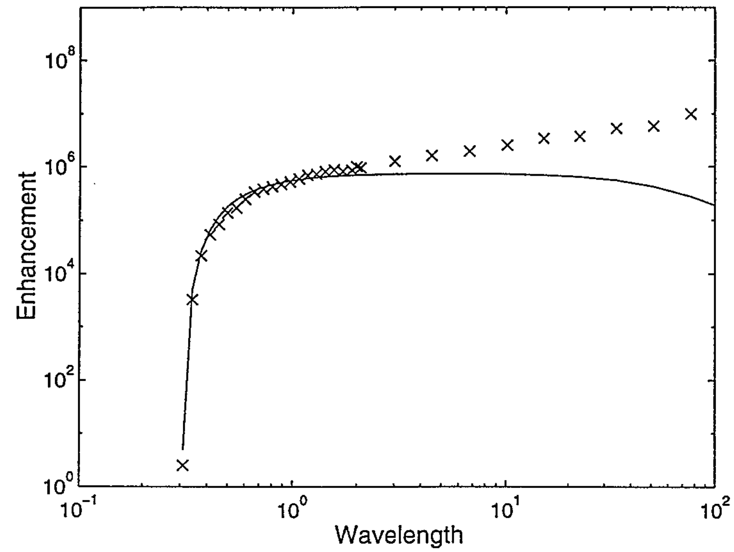

Figure 7. The enhancement factor, G_{RS}, for Raman scattering from a silver semicontinuous film at the percolation threshold (wavelength is in μm). The points are results of the numerical simulations based on the exact formula (6); the solid line represents results of calculations based on the scaling formula (second approximate equality in (6)).

where $E_{2\omega}^{(0)}$ and $E_{2\omega}(\mathbf{r})$ are the macroscopic and local *linear* fields at frequency 2ω. The difference between (7) and (4) is due to the same reason as the difference between (6) and (3) (see the discussion following formula (6) above).

The average enhancement, G_{SHG}, on a silver semicontinuous film as a function of the wavelength at $p = p_c$ is shown in Figure 9a. The enhancement increases toward larger wavelengths where the local fields are higher.

We also calculated the local distributions of the nonlinearly scattered light, with frequency 2ω found from the formula

$$g_{SHG}(\mathbf{r}) = \frac{\varepsilon_{2\omega}(\mathbf{r})}{\varepsilon_{d,2\omega}} \left[\frac{E_\omega(\mathbf{r})}{E_\omega^{(0)}}\right]^2. \tag{8}$$

[For simplicity, we assumed in (8) that there is no "secondary" enhancement for the generated field at frequency 2ω.] The distribution of the local SHG enhancements, $g_{SHG}(\mathbf{r})$, are shown in Figure 9b for $\lambda = 1.5\mu m$ and $\lambda = 20\mu m$ at $p = p_c$. Similar to the case of the SERS local distributions, the peaks in the SHG become much larger with the increase of the wavelength; the spatial separations between them, however, also increase with λ. For the "hot spots" the local enhancement can be giant, reaching values up to 10^{15}, whereas the ensemble-average enhancement is relatively small, as seen from comparison Figs. 9a and 9b.

Huge local enhancements for Raman scattering, SHG, and other nonlinear optical scattering, that significantly exceed the ensemble average enhancements, opens a fascinating possibility to perform Raman and nonlinear spectroscopy for a

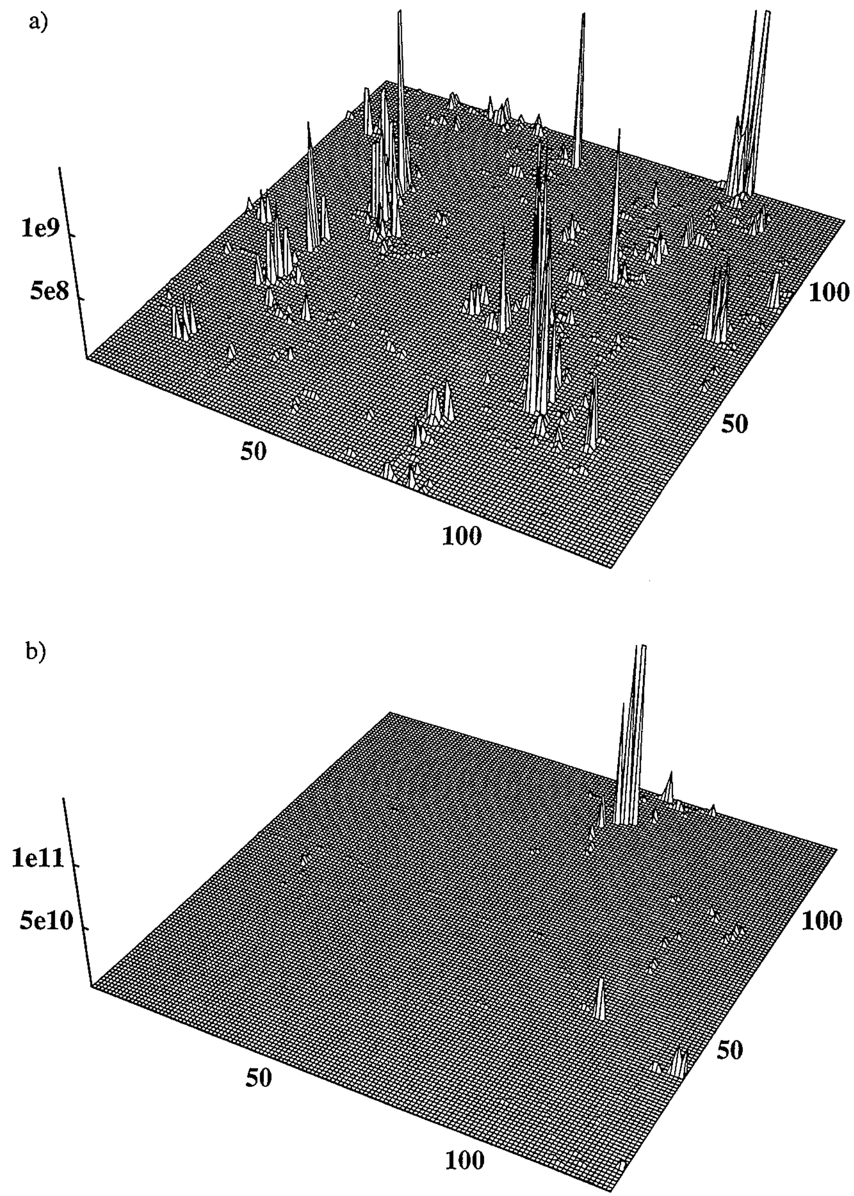

Figure 8. The local SERS distribution on a silver semicontinuous film at the percolation threshold for different wavelengths: a) $\lambda = 1.5\mu m$, and b) $\lambda = 10\mu m$.

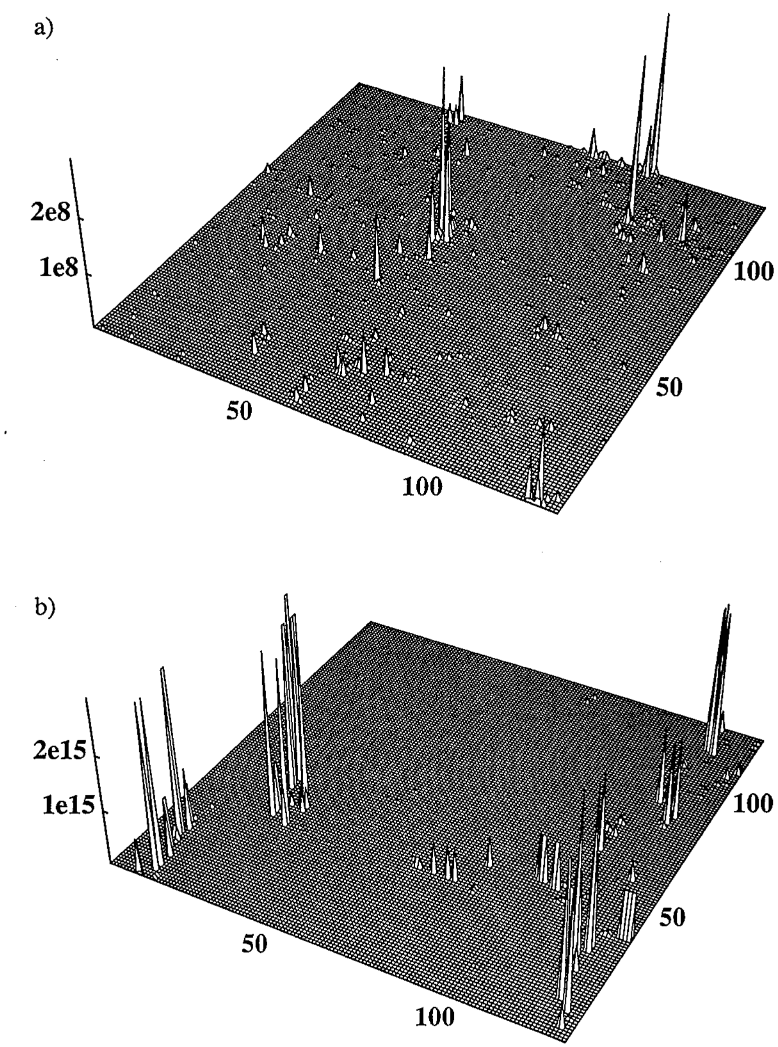

Figure 9. a): The average SHG enhancement, G_{SHG}, on a silver semicontinuous film as a function wavelength at $p = p_c$. The film sizes are 512x512. Distributions of the local SHG enhancements, $g_{SHG}(\mathrm{r})$, for $\lambda = 0.5\mu m$ (b) and $\lambda = 20\mu m$ (c) at $p = p_c$.

single molecule. We note that SERS from a single molecule on a colloidal particle and a fractal aggregate of colloidal particles was recently reported in (*20*).

Conclusions

To conclude, light excitation of objects with fractal morphology, such as aggregates of colloidal particles, self-affine surfaces, and semicontinuous thin films, results in extremely high fields localized in nm-sized "hot spots". This provides huge enhancements for a number of optical phenomena, including Raman scattering, nonlinear refraction and absorption, and second-harmonic generation. The local enhancements exceed the ensemble average by many orders of magnitude.

Acknowledgments

Work was supported by NSF under grant 9500258 and by RFBR under grant 96-02-19331.

Literature Cited

1. *Fractals and Disorder*; Bunde, A., Ed.; North-Holland: 1992; Havlin, S.; Bunde, A. In *Ibid*; p. 97; Alexander, S.; Orbach, R. *J. Phys. (Paris) Lett.* **1982,** *43*, L1625; Rammal, R.; Toulouse, G. *J. Phys. (Paris) Lett.* **1983,** *44*, L13; Sapoval, B.; Gobron, Th.; Margolina, A. *Phys. Rev. Lett.* **1991,** *67*, 2974.
2. Shalaev, V. M. *Phys. Reports* **1996,** *272*, 61.
3. Tsai, D. P.; Kovacs, J.; Wang, Z.; Moskovits, M.; Shalaev, V. M.; Suh, J.; Botet, R. *Phys. Rev. Lett.* **1994,** *72*, 4149; Shalaev, V. M.; Moskovits, M. *Phys. Rev. Lett.* **1995,** *75*, 2451.
4. Markel, V. A.; Shalaev, V. M.; Stechel, E. B.; Kim, W.; Armstrong, R. L.; *Phys. Rev. B* **1996,** *53*, 2425; Shalaev, V. M.; Poliakov, E. Y.; Markel, V. A. *Phys. Rev. B* **1996,** *53*, 2437.
5. Shalaev, V. M.; Botet, R.; Mercer, J.; Stechel, E. B. *Phys. Rev. B* **1996,** *54*, 8235; Poliakov, E. Y.; Shalaev, V. M.; Markel, V. A.; Botet, R. *Opt. Lett.* **1996,** *21*, 1628.
6. Brouers, F.; Blacher, S.; Lagarkov, A.; Sarychev, A. K.; Gadenne, P.; Shalaev, V. M. *Phys. Rev. B* **1997,** *55*, 13234; Gadenne, P.; Brouers, F.; Shalaev, V. M.; Sarychev, A. K. *J. Opt. Soc. Amer. B*, submitted.
7. Jullien R.; Botet, R. *Aggregation and Fractal Aggregates*; World Scientific: Singapore, 1987; Feder, J. *Fractals*; Plenum Press: New York, 1988.
8. Chiarello, R.; Panella, V.; Krim, J.; Thompson, C. *Phys. Rev. Lett.* **1991,** *67*, 3408; Douektis, C.; Wang, Z.; Haslett, T. L.; Moskovits, M. *Phys. Rev. B* **1995,** *51*, 11022; Barbasi, A.-L.; Stanley, H. E. *Fractal Concepts in Surface Growth*; Cambridge U. Press: Cambridge, 1995.
9. Markel, V. A.; Muratov, L. S.; Stockman, M. I., George, T. F. *Phys. Rev. B* **1991,** *43*, 8183; Stockman, M. I.; Pandey, L. N.; Muratov, L. S.; George, T. F. *Phys. Rev. Lett.* **1994,** *72*, 2486; Stockman, M. I.; Pandey, L. N.; Muratov,

L. S.; George, T. F. *Phys. Rev. B* **1995** *51*, 185; Stockman, M. I.; Pandey, L. N.; George, T. F. *Phys. Rev. B* **1996,** *53*, 2183.
10. Stroud, D.; Hui, P. M. *Phys. Rev. B* **1988,** 37, 8719.
11. Boyd, R. W. *Nonlinear Optics*; Academic Press: New York, 1992.
12. Moskovits, M. *Rev. Mod. Phys.* **1985,** *57* , 783; Otto, A.; Mrozek, I.; Grabhorn, H.; Akemann, W. *J. Phys.: Condens. Matter* **1992,** *4*, 1143; *Surface Enhance Raman Scattering*, Chang R. K.; Furtak, T. E., Eds.; Plenum Press: New York, 1982; Stockman, M. I.; Shalaev, V. M.; Moskovits, M.; Botet, R.; George, T. F. *Phys. Rev. B* **1992,** *46*, 2821.
13. Johnson, P. B.; Christy, R. W. *Phys. Rev. B* **1975,** *6*, 4370.
14. Flytzanis, C. *Prog. Opt.* **1992,** *29*, 2539; Ricard. D.; Roussignol, Ph.; Flytzanis, C. *Optics Letters* **1985,** *10*, 511; Hache, F.; Ricard, D.; Flytzanis, C.; Kreibig, U. *Applied Physics A* **1988,** *47*, 347.
15. Rautian, S. G.; Safonov, V. P.; Chubakov, P. A.; Shalaev, V. M.; Stockman, M. I. *JETP Lett.* **1988,** *47*, 243; Butenko, A. V.; *et al.*, *Z. Phys. D* **1990, 17,** 283.
16. Danilova, Yu. E.; Rautian, S. G.; Safonov, V. P. *Bulletin of the Russian Academy of Sciences, Physics* **1996,** *60*, 374; Danilova, Yu. E.; Drachev, V. P.; Perminov, S. V.; Safonov, V. P. *Bulletin of the Russian Academy of Sciences, Physics* **1996,** *60*, 342; Danilova, Yu. E., Safonov, V. P. in: *Fractals Reviews in the Natural and Applied Sciences*; Novak, M. M., Ed.; Chapman & Hall: London, 1995; p. 101; Danilova, Yu. E., Lepeshkin, N. N.; Rautian, S. G.;, Safonov, V. P. *Physica A* **1996,** in press.
17. Zhuravlev, F. A.; Orlova, N. A.; Shelkovnikov, V. V.; Plehanov, A. I.; Rautian, S. G.; Safonov, V. P. *JETP Lett.* **1992,** *56*, 260.
18. Sipe, J. E.; Boyd, R. W. *Phys. Rev. B* (1992) *46*, 1614 (1992); Gehr, R. J.; Fisher, G. L.; Boyd, R. W.; Sipe, J. E. *Phys. Rev. A* **1996,** *53*, 2792; Fisher, G. L.; Boyd, R. W.; Gehr, R. J.; Jenekhe, S. A.; Osaheni, J. A.; Sipe, J. E.; Weller-Brophy, L. A. *Phys. Rev. Lett.* **1995,** *74*, 1871; Boyd, R. W.; Gehr, R. J.; Fisher, G. L.; Sipe, J. E. *Pure Appl. Opt.* **1996,** *5*, 505.
19. Zhang, P.; *et al. Phys. Rev. B*, submitted.
20. Kneipp, K.; *et al. Phys. Rev. Lett.* **1997,** *78*, 1667; Nie, S.; Emory, S. R. *Science* **1997,** *275*, 1102.